ASPECTS OF SUPERCRITICAL TURBULENCE: DIRECT NUMERICAL SIMULATION OF O_2/H_2 AND C_7H_{16}/N_2 TEMPORAL MIXING LAYERS

J. Bellan, N. A. Okong'o and K. G. Harstad
Jet Propulsion Laboratory
California Institute of Technology
Pasadena, CA 91109-8099

Abstract

Results from Direct Numerical Simulations of temporal, supercritical mixing layers for two species systems are analyzed to elucidate species-specific turbulence aspects. The two species systems, O_2/H_2 and C_7H_{16}/N_2, have different thermodynamic characteristics; thus, although the simulations are performed at similar reduced pressure (ratio of the pressure to the critical pressure), the former system is close to mixture ideality and has a relatively high solubility with respect to the latter, which exhibits strong departures from mixture ideality. Due to the specified, smaller initial density stratification, the C_7H_{16}/N_2 layers display higher growth and increased global molecular mixing as well as larger turbulence levels. However, smaller density gradients at the transitional state for the O_2/H_2 system indicate that on a local basis, the layer exhibits an enhanced mixing, this being attributed to the increased solubility and to mixture ideality. These thermodynamic features are shown to affect the irreversible entropy production (i.e. the dissipation), which is larger for the O_2/H_2 layer and is primarily concentrated in high density-gradient magnitude regions that are distortions of the initial density stratification boundary. In contrast, the regions of largest dissipation in the C_7H_{16}/N_2 layer are located in high density-gradient magnitude regions resulting from the mixing of the two fluids.

1 INTRODUCTION

Current interest in supercritical turbulent fluid behavior stems from the need to improve and control liquid rocket propulsion and from the necessity to predict the behavior of fuel in advanced gas turbine and Diesel engines. In the first case the oxidant/fuel system is O_2/H_2, whereas in the second situation it is air/hydrocarbons. A simplified description of the sequence of events in one of these combustion chambers is as follows: either the oxidizer or the fuel is injected in the chamber, and irrespective of the exact injection configuration it disintegrates, mixes with the surrounding fluid in a highly turbulent manner while being ignited, with ensuing combustion producing a variety of chemical species. From this description, it is immediately clear that fluid disintegration and turbulence play a crucial role in determining the size and composition of the parcels of fluid entering in contact, and consequently the efficiency of combustion.

In all practical situations mentioned above, the disintegrating fluid enters a chamber that is pressurized above the fluid critical pressure of the injected fluid. Therefore, the fluid becomes immediately supercritical. A substance is in a supercritical state when it is at a thermodynamic pressure, p, **or** temperature, T, exceeding its critical value[1] (indicated here by subscript c). What truly characterizes the supercritical state is the impossibility of a two phase region. Indeed, when the reduced pressure, $p_r \equiv p/p_c > 1$ **or** the reduced temperature $T_r \equiv T/T_c > 1$, in the (p, T) plane there is no longer the possibility of a two phase (i.e. gas/liquid) region, and instead there is only a single-phase region[2] . The general term for the substance is fluid, i.e. neither a gas nor a liquid.

Supercritical fluid disintegration is a process essentially different from the much studied spray atomization that involves the breakup of a liquid into a multitude of drops. Liquid breakup relies on physical mechanisms involving the surface tension, and therefore it is an appropriate concept only when a surface tension does indeed exist. In contrast to atomization, past the critical point of the fluid, disintegration assumes the aspect of what Chehroudi et al.[3] call 'fingers', or 'comb-like structures' at transcritical conditions, having an increasingly gaseous appearance with increasing p; their experiments were conducted with N_2/N_2,$N_2/(CO+N_2)$, He/N_2 and O_2/N_2. Similar experimental evidence was produced by Mayer et al.[4,5] for O_2 disintegration. Related to the present study, Raman scattering measurements of the radial density in free N_2 jets at 4 MPa by Oschwald and Schik[6] show sharp profiles independent of the injection temperature, indicating the occurrence of sharp density gradients. It will be shown below that these regions of sharp density gradients, which are indeed one of the distinctive optical features of species mixing under supercritical conditions, are also intimately related to turbulence. Moreover, it will be shown that according to the specific thermodynamics of the mixture, turbulence is influenced by regions of high density-gradient magnitude originating from different processes.

In this paper we adopt a representative binary species system (C_7H_{16}/N_2) to study the mixing of the air/hydrocarbon system, which is currently too complex for detailed fundamental simulations. This approximation enables the comparison, in the context of mixing layers, of two very different binary species systems; such a comparison has already been performed in the realm of drop behavior[7] but was restricted to laminar flows. The two systems compared are O_2/H_2 and C_7H_{16}/N_2 and the properties of these species are listed in Table 1. Results from Direct Numerical Simulations (DNS) described elsewhere [8–10] are here compared, leading to new insights into supercritical turbulence.

2 CONSERVATION EQUATIONS

For a binary mixture, the conservation equations are

$$\frac{\partial \rho}{\partial t} + \frac{\partial (\rho u_j)}{\partial x_j} = 0, \tag{1}$$

$$\frac{\partial (\rho u_i)}{\partial t} + \frac{\partial (\rho u_i u_j + p\delta_{ij})}{\partial x_j} = \frac{\partial \tau_{ij}}{\partial x_j}, \tag{2}$$

$$\frac{\partial (\rho Y_2)}{\partial t} + \frac{\partial (\rho Y_2 u_j)}{\partial x_j} = -\frac{\partial j_{2j}}{\partial x_j}, \tag{3}$$

$$\frac{\partial (\rho e_t)}{\partial t} + \frac{\partial [(\rho e_t + p) u_j]}{\partial x_j} = -\frac{\partial q_{IKj}}{\partial x_j} + \frac{\partial \tau_{ij} u_i}{\partial x_j}, \tag{4}$$

where x is a Cartesian coordinate, t is time, ρ is the density, u_i is the i^{th} component of the velocity, $e_t = e + u_i u_i/2$ is the total energy (i.e. internal energy, e, plus kinetic energy), Y_2 is the mass fraction of the heavier species (the mass fraction of the lighter one is $Y_1 = 1 - Y_2$). Furthermore, $\mathbf{q}_{IK}$ is the Irwing-Kirkwood (subscript IK) form of the heat flux vector (see Sarman and Evans[11]), $\mathbf{j}_2$ is the heavier species mass flux vector and τ_{ij} is the Newtonian viscous stress tensor

$$\tau_{ij} = \mu \left[\frac{\partial u_i}{\partial x_j} + \frac{\partial u_j}{\partial x_i} - \frac{2}{3} \frac{\partial u_k}{\partial x_k} \delta_{ij} \right], \tag{5}$$

where δ_{ij} is the Kronecker delta function, and μ is the mixture viscosity that is in general a function of the thermodynamic state variables. The mass flux and heat flux are given by

$$j_{2j} = -\left[j'_{2j} + (\alpha_{IK} - \alpha_h) Y_2 Y_1 \frac{\rho D}{T} \frac{\partial T}{\partial x_j} \right], \tag{6}$$

$$q_{IKj} = -\lambda'_{IK}\frac{\partial T}{\partial x_j} - \alpha_{IK}R_uT\frac{m}{m_2m_1}j'_{2j}, \tag{7}$$

$$j'_{2j} = \rho D\left[\alpha_D\frac{\partial Y_2}{\partial x_j} + \frac{Y_2Y_1}{R_uT}\frac{m_2m_1}{m}\left(\frac{v_{,2}}{m_2} - \frac{v_{,1}}{m_1}\right)\frac{\partial p}{\partial x_j}\right], \tag{8}$$

$$\alpha_h = \frac{1}{R_uT}\frac{m_2m_1}{m}\left(\frac{h_{,2}}{m_2} - \frac{h_{,1}}{m_1}\right). \tag{9}$$

The notation in eqs. 6 - 9 is as follows: D is the binary diffusion coefficient; α_D is the mass diffusion factor, which is a thermodynamic quantity; m_α is the molar mass of species α; $m = m_1X_1 + m_2X_2$ is the mixture molar mass where the molar fraction $X_\alpha = mY_\alpha/m_\alpha$; $v_{,\alpha} = (\partial v/\partial X_\alpha)_{T,p,X_{\beta(\beta\neq\alpha)}}$ is the partial molar volume and $h_{,\alpha} = (\partial h/\partial X_\alpha)_{T,p,X_{\beta(\beta\neq\alpha)}}$ is the partial molar enthalpy; $v = X_1v_{,1} + X_2v_{,2}$, is the molar volume related to the density by $v = m/\rho$; $h = X_1h_{,1} + X_2h_{,2}$ is the molar enthalpy; R_u is the universal gas constant and λ'_{IK} is a thermal conductivity defined from the transport matrix through

$$\lambda'_{IK} = \lambda + X_1X_2\,\alpha_{IK}\,\alpha_{BK}R_u\rho D/m, \tag{10}$$

with $\lim_{p\to 0}\lambda = \lambda_{KT}$ as discussed in Harstad and Bellan[12] , where the subscript KT refers to Kinetic Theory. The transport coefficients associated with the Soret (in the molar fluxes) and the Dufour (in the heat flux) terms of the transport matrix are α_{BK} and α_{IK}, which are the thermal diffusion factors corresponding to the IK and the Bearman-Kirkwood (subscript BK) forms of the heat flux (see Sarman and Evans[11]). These transport coefficients are characteristic of each particular species pairs and they obey the relationship[12]

$$\alpha_{BK} = \alpha_{IK} - \alpha_h. \tag{11}$$

Additionally, $\lim_{p\to 0}\alpha_{IK} \neq \alpha_{KT}$ and $\lim_{p\to 0}\alpha_{BK} = \alpha_{KT}$.

To solve the system of equations above, one must specify the equation of state (EOS) and the transport properties (or equivalently specify the non-dimensional numbers relating the transport properties).

3 EQUATION OF STATE

The pressure can be calculated from the well-known Peng-Robinson (PR) EOS given T and the PR molar volume, v_{PR}, as

$$p = \frac{R_uT}{(v_{PR} - b_m)} - \frac{a_m}{(v_{PR}^2 + 2b_mv_{PR} - b_m^2)}, \tag{12}$$

where a_m, b_m are functions of T and X_α[8–10] . Due to the inaccuracy of eq. 12 at high pressures[1] , v_{PR} may differ significantly from the actual molar volume v. For the C_7H_{16}/N_2 system these inaccuracies are minor, however, this is not the case for O_2/H_2. Therefore, for improved accuracy in the O_2/H_2 case, we used a modified PR EOS in which both v_{PR}, and the volume shift[13]

$$v_S = v - v_{PR} \tag{13}$$

were calculated from the PR EOS given p, T and X_α. More details on this calculation can be found elsewhere[10] .

The mass diffusion factor, α_D, is calculated from the fugacity coefficients, φ_α, through

$$\alpha_D = 1 + X_\alpha\frac{\partial \ln(\varphi_\alpha)}{\partial X_\alpha} \tag{14}$$

and portrays departures from mixture ideality (i.e. $\alpha_D = 1$).

4 TRANSPORT COEFFICIENTS

DNS are calculations wherein both the Kolmogorov and Batchelor scales must be resolved. To ensure that this requirement is satisfied, contour plots of μ, the Schmidt number, Sc, and the Prandtl number, Pr, based on accurate species transport properties calculated as in Harstad and Bellan[14] were produced. Based on these contour plots, the transport properties were correlated as

$$\mu = \mu_R \left(\frac{T}{(T_1 + T_2)/2} \right)^n, \tag{15}$$

where T is in degrees Kelvin, $n = 0.75$ for O_2/H_2 and $n = 0.7$ for C_7H_{16}/N_2. For O_2/H_2 in the range 200K to 800K at $p = 100$atm, which is applicable to liquid rocket engines,

$$Sc \equiv \frac{\mu}{\rho \alpha_D D} = (1.334 - 0.668 Y_O - 0.186 Y_O^2 - 0.268 Y_O^6) \left[1 + \left(\frac{88.6}{T} \right)^{1.5} \right], \quad \mathrm{Pr} \equiv \frac{\mu C_p/m}{\lambda} = \frac{1.335}{T^{0.1}}, \tag{16}$$

while for C_7H_{16}/N_2 in the range 500 K$\leq T \leq$1100 K, 40 atm $\leq p \leq$80 atm

$$Sc = 1.5 - Y_h, \qquad \mathrm{Pr} = \frac{Sc}{2\exp(-3Y_h/2)}. \tag{17}$$

The particular thermodynamic range chosen for C_7H_{16}/N_2 enables simulations pertinent to both diesel and gas turbine engine studies. In eq. 15, μ_R is a reference viscosity, the reference temperatures T_1 (upper, H_2 or N_2, stream) and T_2 (lower, O_2 or C_7H_{16}, stream) correspond to the free stream temperatures for mixing layer simulations, and the subscripts O and h in eqs. 16 and 17 denote oxygen and heptane, respectively.

The value of μ_R is determined by the specified value of the initial Reynolds number Re_0 (see below), chosen so as to enable the resolution of all relevant length scales.

The thermal diffusion factor is selected as in Harstad and Bellan[14,15] with $\alpha_{BK} = 0.2$ for O_2/H_2, and α_{IK} is calculated from eq. 11. For the C_7H_{16}/N_2 system, the value of $\alpha_{IK} = 0.1$ is employed, as determined by Harstad and Bellan[12] , and α_{BK} is calculated from eq. 11.

5 CONFIGURATION AND BOUNDARY CONDITIONS

The temporally developing mixing layer configuration is depicted as an example in Fig. 1 for O_2/H_2, showing the definition of the streamwise (x_1), cross-stream (x_2) and spanwise (x_3) coordinates. The layer is not symmetric in extent in the x_2 direction, having found in our simulations that the layer growth is considerably larger in the lighter gas (H_2 or N_2) side. The freestream density ($\rho_1$or ρ_2) is calculated for each pure species at its freestream temperature (T_1 or T_2) and at the initial uniform pressure (p_0). The vorticity thickness is defined as $\delta_\omega(t) = \Delta U_0 / \left(\partial \langle u_1 \rangle / \partial x_2 \right)_{max}$ where $\langle u_1 \rangle$ is the $(x_1 - x_3)$ planar average velocity in the streamwise direction, and $\Delta U_0 = U_1 - U_2$ is the velocity difference across the layer. The simulation is initiated with four streamwise vortices, which pair twice to produce an ultimate vortex. The choice of U_1 and U_2 for a real fluid

$$U_1 = 2 M_{c,0} a_{s_1} \left[1 + \left(\frac{a_{s_1}}{a_{s_2}} \right) \sqrt{\frac{\rho_1 Z_1}{\rho_2 Z_2}} \right]^{-1}, \qquad U_2 = -\sqrt{\frac{\rho_1 Z_1}{\rho_2 Z_2}} U_1, \tag{18}$$

was made with the intent of keeping the ultimate vortex stationary in the computational domain[8] . Here $M_{c,0}$ is the convective Mach number and $Z = p/(\rho T R_u/m)$ is the compression factor indicating departures from the perfect gas behavior (i.e. $Z = 1$). The specification of $M_{c,0}$ therefore determines ΔU_0. Given the initial streamwise velocity profile u_1 based on U_1 and U_2, $\left(\partial \langle u_1 \rangle / \partial x_2 \right)_{max}$ and hence $\delta_{\omega,0} \equiv \delta_\omega(0)$ are calculated. The specified value of the initial flow Reynolds number,

$$\mathrm{Re}_0 = \frac{0.5(\rho_1 + \rho_2) \Delta U_0 \delta_{\omega,0}}{\mu_R} \tag{19}$$

is then used to calculate μ_R.

The boundary conditions are periodic in the streamwise and spanwise directions, and of outflow type for real gas in the cross-stream direction, as derived by Okong'o and Bellan[16] . The outflow type conditions are essential to maintain stability since the initial perturbation causes large pressure waves that must be allowed out of the domain with minimal reflection.

6 NUMERICS

The conservation equations are numerically solved using a fourth-order explicit Runge-Kutta time integration and a sixth-order compact scheme for spatial derivatives[17] . Time stability is achieved by filtering the conservative variables every five time steps in the interior, in each spatial direction alternately, using an eighth-order filter. Since high-order boundary filters are unstable, no filtering is applied at the non-periodic (x_2) boundaries. The computations were parallelized using three-dimensional domain decomposition and message passing. The tridiagonal solver for the compact derivative scheme was efficiently parallelized[18] and the simulations were performed on an SGI Origin 2000 supercomputer, using 64 processors.

In our solution protocol, once p, T, and X_α are calculated, ρ and e are calculated from the EOS. To calculate p and T from the known e and X_α, for O_2/H_2 we iterate at each time step[10] , whereas for C_7H_{16}/N_2 we use an energy fit[9] .

The absence of small scale fluctuations in the dilatation field, $\nabla \cdot u$, is well known to be a reasonable indicator of good resolution. The appropriate resolution of all scales is checked by visual inspection of $\nabla \cdot u$, which shows no such fluctuations. Furthermore, energy spectra based on velocity fluctuations were calculated and were shown to display an eight to ten order of magnitude ratio between the large and small scales, showing that the overwhelming energy is in the large scales, and thus that the simulations are well resolved.

7 INITIAL CONDITIONS

The interest is here in comparing results from different DNS in order to elucidate species-system-specific turbulence aspects. All simulations to be compared would have the same non-dimensional dynamical initial conditions, except for Re_0. The thermodynamic initial conditions (p, T_1, T_2) are chosen for the C_7H_{16}/N_2 system to be in the regime of relevance to gas turbine and diesel engines (60 atm, 1000K, 600K), whereas those for the O_2/H_2 system are selected as close to the liquid rocket conditions as computationally feasible because the quite different thermodynamic properties of the two mixtures (as encapsulated by their respective equations of state) do not permit the matching of the thermodynamic initial conditions. For example, the initial pressure (which must be uniform) is such that p_r in the heavier gases is similar (2.22 for C_7H_{16} and 2.01 (i.e. 100 atm) for O_2), however it is dissimilar for the lighter gases (1.78 for N_2 and 7.89 for H_2). Attempting to match the initial reduced temperatures of the two systems (T_r=1.11 and 7.92 for the C_7H_{16} and N_2 streams respectively), would require T_2=172K and T_1=261K for the O_2/H_2 layer, for which ρ_2/ρ_1 would be 58.30; the resolution requirements for this density stratification do not presently permit DNS. An alternative strategy would be to match a dimensionless temperature, such as $|T_2 - T_1|/T_2$. For the C_7H_{16}/N_2 layer, $|T_2 - T_1|/T_2$ =0.667; either choice of T_2=172K (T_1=287K) or T_1=261K (T_2=157K) for the O_2/H_2 layer leads to an excessively large density stratification, as illustrated in Fig. 2a which shows ρ_2/ρ_1 over a range of T_1 and T_2 at p =100 and 400 atm. On the other hand, matching the initial density stratification of 12.88 for C_7H_{16}/N_2 system would require H_2 to be colder than O_2, which is the opposite of the situation encountered in liquid rocket chambers; in fact, over the regime of interest, having O_2 be colder than H_2 means having a density stratification larger than 12.88. Therefore, the conditions for the O_2/H_2 simulations are chosen to have a more modest $|T_2 - T_1|/T_2$=0.5, with a computationally tractable ρ_2/ρ_1=24.40, and mean stream temperatures (T_1=600K, T_2=400K) that are relevant to liquid rocket chambers, while satisfying the requirement that the O_2 be the colder fluid.

The effect of the density stratification on the stability of the layer, and hence its response to perturbations, was thoroughly investigated by Okong'o and Bellan[19] for real gases, and applied to the C_7H_{16}/N_2 system

under supercritical conditions. The same formalism was applied by Okong'o et al.[10] to the O_2/H_2 system. In these studies, two-dimensional inviscid stability analyses were conducted for the same error function mean profiles used in the present simulations, using various freestream conditions to produce stratifications of 1, 12.88 and 24.40. For the stability analyses, the freestream mean velocity was specified as

$$\bar{u}_1(\infty) = U_1; \quad \bar{u}_1(-\infty) = U_2 \tag{20}$$

and perturbations were imposed through

$$\Delta u_i = \hat{u}_i(x_2)\exp\left[i\alpha(x_1 - ct)\right], \quad \Delta p = \hat{p}(x_2)\exp\left[i\alpha(x_1 - ct)\right], \quad \Delta\rho = \hat{\rho}(x_2)\exp\left[i\alpha(x_1 - ct)\right], \tag{21}$$

where α is real and c is complex, the hat denotes the perturbation amplitudes, all of which are functions of x_2 only, and the physical quantities are obtained by taking the real part of the complex quantities. The stability curves for O_2/H_2 and C_7H_{16}/N_2 at the same ρ_2/ρ_1=12.88 are plotted in Fig 2b, along with those of O_2/O_2 and C_7H_{16}/C_7H_{16} at ρ_2/ρ_1=1. The freestream conditions are listed for O_2/O_2 and O_2/H_2 in Table 2 and for C_7H_{16}/C_7H_{16} and C_7H_{16}/N_2 in Table I and III of Okong'o and Bellan[19] ; all for $M_{c,0}$=0.4. Since the mean velocity, density and speed of sound have the same profiles for O_2/H_2 and C_7H_{16}/N_2, the stability curves could be expected to be similar for the same initial density stratification and $M_{c,0}$. However, as illustrated in Fig. 2b, discrepancies arise because, due to the different fluid properties, the freestream Mach numbers are different. Generally, the most unstable wavelengths are slightly longer for the O_2/H_2 mixture. More importantly, with increasing density stratification the most unstable wavelength increases and its amplitude decreases, indicating that the resistance of the layer to perturbations increases.

The simulations are started with error-function profiles for the mean streamwise velocity, mass fraction and temperature, upon which are imposed streamwise and spanwise vorticity perturbations[20,21] :

$$\omega_1(x_2, x_3) = F_{3D}\frac{\lambda_1 \Delta U_0}{\Gamma_1} f_2(x_2) f_3(x_3), \quad \omega_3(x_1, x_2) = F_{2D}\frac{\lambda_3 \Delta U_0}{\Gamma_3} f_1(x_1) f_2(x_2), \tag{22}$$

where Γ_1 and Γ_3 are the circulations,

$$f_1(x_1) = A_0\left|\sin\left(\frac{\pi x_1}{\lambda_1}\right)\right| + A_1\left|\sin\left(\frac{\pi x_1}{2\lambda_1}\right)\right| + A_2\left|\sin\left(\frac{\pi x_1}{4\lambda_1}\right)\right| + A_3\left|\sin\left(\frac{\pi x_1}{8\lambda_1} - \frac{\pi}{2}\right)\right|, \tag{23}$$

$$f_2(x_2) = \exp\left[-\pi\left(\frac{x_2}{\delta_{\omega,0}}\right)^2\right], \quad f_3(x_3) = B_0\sin\left(\frac{2\pi x_3}{\lambda_3}\right) + B_1\sin\left(\frac{\pi x_3}{L_3}\right). \tag{24}$$

We use F_{2D}=0.1, A_0=1, A_1=0.5, A_2=A_3=0.35 for the streamwise perturbations, and F_{3D}=0.05, B_0=1 and B_1=0.025 for the spanwise perturbations. The wavelength of the perturbation is λ_1=7.29$\delta_{\omega,0}$ (the most unstable wavelength for incompressible flow) and λ_3=0.6λ_1, following Moser and Rogers[21] . The grid is chosen for all simulations so as to accommodate four wavelengths in the streamwise and spanwise directions, and the evolution of the layer is meant to encompass rollup and two pairings of the initial spanwise vortices.

8 RESULTS

All simulations to be compared have the same dynamical initial conditions ($M_{c,0}$ and vorticity perturbation amplitudes) except for Re_0, which are listed in Table 3. For R600oh in Table 3, the value of Re_0 is chosen to emulate that of R600hn, which led to a transitional state[9] ; however, R600oh did not achieve a transitional state. The larger Re_0=750 of the second O_2/H_2 simulation did lead to transition. The lack of transition of R600oh was due to the higher initial density stratification of 24.40 compared to the much smaller value of 12.88 employed in R600hn.

8.1 GLOBAL GROWTH AND ROTATIONAL CHARACTERISTICS

A fundamental characteristic of mixing layers is their growth. Although many definitions of growth exist,

Cortesi et al.[22] showed that several such measures, including the momentum thickness, are qualitatively similar. Here, we define the momentum thickness as

$$\delta_m = \frac{-1}{(\theta_1 - \theta_2)^2} \int_{-L_{2,\min}}^{L_{2,\max}} (\theta_2 + \langle \rho u_1 \rangle)(\theta_1 + \langle \rho u_1 \rangle) dx_2 \tag{25}$$

with $\theta_1 = \langle \rho u_1 \rangle_{x_2 = L_{2,\max}}$ and $\theta_2 = \langle \rho u_1 \rangle_{x_2 = L_{2,\min}}$, where $L_{2,\min} = -L_2/3$ and $L_{2,\max} = 2L_2/3$. While the growth is mostly a consequence of entrainment, the product thickness defined as $\delta_p = \int\int\int_V \rho Y_p dV$ in mass units, where $Y_p = 2\min(Y_1, Y_2)$, is a direct consequence of molecular mixing as also explained by Cortesi et al.[22] . $\delta_m/\delta_{\omega,0}$ is illustrated versus the non-dimensional time $t^* = t\Delta U_0/\delta_{\omega,0}$ in Fig. 3a for all simulations. All layers roll up and pair twice. However, the C_7H_{16}/N_2 layers display a drastic increase in $\delta_m/\delta_{\omega,0}$ after the first pairing, whereas their O_2/H_2 counterpart tend to grow more slowly. The drastic growth of the C_7H_{16}/N_2 layers compared to the O_2/H_2 ones is attributed to the smaller initial density stratification. This is also the reason that the C_7H_{16}/N_2 layers exhibit a plateau after the second pairing, this being a manifestation of forcing; no such effect is discernible for the more highly-density-stratified O_2/H_2 layers, which are more resistant to entrainment and seem to grow more linearly. Not surprisingly, $\delta_p/\delta_{p,0}$, depicted in Fig. 3b displays a much larger growth for C_7H_{16}/N_2 than for O_2/H_2 as a function of t^*, meaning that global molecular mixing is much more intense.

Illustrated in Fig. 3c is the non-dimensional positive spanwise vorticity, $\langle\langle \omega_3^+ \rangle\rangle (\delta_{\omega,0}/\Delta U_0)$, which is indicative of small turbulent scale formation considering that due to the initial mean velocity profile, the initial spanwise vorticity is negative. The non-dimensional enstrophy, $\langle\langle \omega_i \omega_i \rangle\rangle (\delta_{\omega,0}/\Delta U_0)^2$, where $\boldsymbol{\omega} = \nabla \times \mathbf{u}$ is the vorticity and $\langle\langle\rangle\rangle$ denotes volume averaging, is shown in Fig. 3d and is a manifestation of stretching and tilting, which is the mechanism primarily responsible for the formation of small scales. For all simulations, $\langle\langle \omega_3^+ \rangle\rangle (\delta_{\omega,0}/\Delta U_0)$ increases from the null value once the layer rollup is completed; however, a reduced augmentation rate is displayed by the O_2/H_2 layers (with particular significance for the R600oh and R600hn layers, which have the same Re_0), corresponding to the reduced layer growth. All curves exhibit local peaks at the first pairing; however, $\langle\langle \omega_3^+ \rangle\rangle (\delta_{\omega,0}/\Delta U_0)$ increases following the first pairing of the C_7H_{16}/N_2 layers but decreases for the transitional O_2/H_2 layer. Moreover, $\langle\langle \omega_3^+ \rangle\rangle (\delta_{\omega,0}/\Delta U_0)$ is considerably smaller for the transitional O_2/H_2 layer compared to the equivalent C_7H_{16}/N_2 ones, indicating that turbulence for the former is substantially reduced with respect to the latter. The enstrophy variation is consistent with this physical picture, displaying reduced levels for the O_2/H_2 layer when compared to the C_7H_{16}/N_2 ones.

To understand these reduced turbulence levels and growth of the O_2/H_2 layers compared to the C_7H_{16}/N_2 ones, several fundamental aspects of the flow are examined below.

8.2 VISUALIZATIONS OF THE DENSITY GRADIENT MAGNITUDE AT TRANSITION

One of the most distinctive features of supercritical mixing layers is the existence of high density-gradient magnitude (called further herein by the acronym HDGM) regions. These regions have been identified in experiments with turbulent supercritical jets[3,6] and in both pre-transitional[8,10,19] and transitional[9,10,19] supercritical mixing layers simulations. Movie animations of the $|\nabla\rho|$ timewise evolution show that the origin of these regions is not only from the distortion of the initial boundary between the two fluid species, but also from the mixing between the two species; this conclusion holds independent of the binary system of species. Because the most apparent difference in initial conditions between the simulations conducted with each of the binary species systems is in the initial density stratification, it is important to examine and compare $|\nabla\rho|\,\delta_{\omega,0}/\Delta\rho_0$, where $\Delta\rho_0 = \rho_2 - \rho_1$, at the transitional states.

Depicted in Fig. 4 is $|\nabla\rho|\,\delta_{\omega,0}/\Delta\rho_0$ in the braid plane (BP) and in the between-the-braid plane (BTBP) for the R750oh and R600hn layers; these two layers are compared because they have a similar magnitude of the momentum thickness based Reynolds number, $\mathrm{Re}_m = \mathrm{Re}_0\,\delta_m/\delta_{\omega,0}$, at the transitional state (see Table 3). In contrast to the smooth aspect of the R750oh HDGM regions, their R600hn equivalent are very convoluted, consistent with the larger turbulence level detected from the comparison of the global quantities. Although the R750oh layer is initiated with about the same $|\nabla\rho|\,\delta_{\omega,0}/\Delta\rho_0$ value (albeit with about twice the density stratification) of R600hn, $|\nabla\rho|\,\delta_{\omega,0}/\Delta\rho_0$ at transition is about a factor of 2 smaller

than that of R600hn. This is attributed to the much wider HDGM regions in the former case compared to the latter produced by the much larger solubility of H_2 into O_2 than of N_2 into C_7H_{16}, and by the much better molecular mixing as the former mixture is nearly ideal whereas the latter mixture is far from ideality (i.e. $0.5 < \alpha_D < 1$)[9] . Thus, although the global molecular mixing, represented by $\delta_p/\delta_{p,0}$, is more intense for the C_7H_{16}/N_2 layer, the local molecular mixing is stronger for the O_2/H_2 layer.

Since it has been observed that a sharp density stratification is very effective at damping turbulent eddies[23,24] , being qualitatively similar to a rigid flat plate, it is clear that, other conditions being similar, the more widespread these regions are, the more damping of turbulent eddies will occur. To further understand the relationship between the HDGM regions and turbulence, we examine below the characteristics of the dissipation.

8.3 IRREVERSIBLE ENTROPY PRODUCTION (DISSIPATION) AT TRANSITION

Okong'o and Bellan[25] have shown that if g denotes the rate of irreversible entropy production

$$g = g_{visc} + g_{temp} + g_{mass} \,, \tag{26}$$

$$g_{visc} = \frac{\mu}{T}\left(2S_{ij}S_{ij} - \tfrac{2}{3}S_{kk}S_{ll}\right), \quad g_{temp} = \frac{\lambda}{T^2}\frac{\partial T}{\partial x_j}\frac{\partial T}{\partial x_j}, \quad g_{mass} = \frac{1}{Y_1 Y_2 \rho D}\frac{R_u m}{m_1 m_2} j_{2j} j_{2j} \,, \tag{27}$$

$$S_{ij} = \frac{1}{2}\left(\frac{\partial u_i}{\partial x_j} + \frac{\partial u_j}{\partial x_i}\right), \tag{28}$$

where according to eqs. 6 - 8, g_{mass} contains the departure from mixture non-ideality (through j_{2j}), $\propto \alpha_D$, and the Soret term, $\propto \alpha_{BK}$. Illustrated in Fig. 5 is g for R750oh and R600hn in the same planes as in Fig. 4. As previously discussed[9,10] , the regions of highest g magnitude are located within the HDGM regions; this can be clearly seen by comparing Figs. 4 and 5. Noteworthy, the magnitude of g is larger in both the BP and the BTBP region for the R750oh simulation, confirming the idea of larger activity in the dissipation for the O_2/H_2 layer; this is the mechanism responsible for the lower turbulence levels of the O_2/H_2 layer. Also confirmed is the conclusion from the HDGM analysis that the regions of dissipation are much more wide spread for the R750oh than for the R600hn layer, leading to the higher dissipation. This means that as far as the dissipation is concerned, although both the extent and the strength of the HDGM regions matter, the extent rather than the strength (measured by the $|\nabla\rho|\,\delta_{\omega,0}/\Delta\rho_0$ magnitude) appears to be more important for the situation examined here.

Scrutiny of the plots in Fig. 5 together with movies of the $|\nabla\rho|$ evolution reveals another major difference between the dissipation in the R750oh and R600hn layers. In the former, the major contribution to the dissipation is from the lower layer regions located on the side of the heavier species stream; these regions correspond to the distortion of the initial density stratification boundary. In contrast, for the R600hn layer, the largest dissipation occurs in the upper stream, which corresponds to the lighter stream; these locations are within HDGM regions originating from fluid mixing rather than the original density stratification. To understand this essentially different aspect of the dissipation, we examined the budget of g in $(x_1 - x_3)$ homogeneous planes according to eqs. 26 and 27.

Homogeneous-plane average and RMS plots of the g_{visc}, g_{mass} and g_{temp} contributions to g are displayed in Figs. 6. In all plots, contributions from g_{mass} dominate those from g_{visc} and g_{temp}. Considering the average (Figs. 6a and 6c), g_{mass} is larger than each of the other contributions by a factor of 6 - 7 for the O_2/H_2 layer, whereas for the C_7H_{16}/N_2 layer, this ratio is about 3 for g_{temp} and about a two orders of magnitude for g_{visc}. These considerations about the ratio of terms in eq. 26 is also valid for the RMS. Therefore, it appears that the viscous dissipation plays a much smaller role for C_7H_{16}/N_2 than for O_2/H_2.

Examining the average plots (Figs. 6a and 6c), the largest peaks in g_{mass} are located for the R750oh simulation on the O_2 side of the layer, corresponding to the HDGM regions, and at the boundary of the two species, corresponding to large gradients in the mass fractions[10] ; the secondary peaks in the H_2 region also correspond to the HDGM region. For the R600hn simulation, the largest peaks occur on the N_2 side,

where the mass fraction gradients are large[9] .

A similar examination of the RMS (Figs. 6b and 6d) reveals that the major peak for R750oh corresponds to the boundary between species, with secondary peaks on either side corresponding to the HDGM regions. In contrast, for the R600hn simulation, the sharp peaks on the heptane side of the layer correspond to isolated pockets of strong dissipation that can be seen in Figs. 5c and 5d.

Since the mass fraction gradients play such an important role in the dissipation, it is worth exploring the phenomena responsible for their persistence, or their smearing. The inherent mixing ability of the O_2/H_2 system (both solubility and mixture ideality) smears the mass fraction gradients[14] and is responsible for weak HDGM regions originating from mixing, as shown in Figs. 4a and 4b. For this reason, the associated dissipation in Figs. 5a and 5b is correspondingly weak. In contrast, the C_7H_{16}/N_2 system being far from mixture ideality and comparatively much less soluble, tends to maintain strong gradients in the mixing region, as seen on Figs. 4c and 4d; this result was also found for C_7H_{16} drops in N_2[26] . The strong density gradients enhance dissipation in those regions. Therefore, we find again that the specific turbulent aspects of each binary species layer are strongly related to the particular thermodynamic features of the mixture.

9 CONCLUSIONS

Several databases obtained from previous Direct Numerical Simulations are compared to investigate the mixture-dependent aspects of supercritical turbulence. The simulations are of three-dimensional temporal mixing layers composed of a heavy fluid that is initially in the lower stream and a lighter fluid that constitutes initially the upper stream. The two species systems investigated are O_2/H_2 and C_7H_{16}/N_2, and the initial conditions are such that all results are from simulations performed at approximately the same reduced pressure of 2 with respect to the pure heavier species. For the first species system, the thermodynamic regime of the simulation is such that the mixture is asymptotically close to ideal, whereas the second mixture experiences strong departures from ideality. A stability analysis conducted for the O_2/H_2 system showed that at the same density stratification, the stability curve is similar to the C_7H_{16}/N_2 system. It is also shown that at high pressure, as O_2 is at lower temperatures, the stratification increases dramatically.

The layer is initially perturbed to initiate entrainment, rollup and pairing, and the same perturbation wavelength is used in all simulations. Each layer originally consists of four vortices that undergo two pairings to form a single ultimate vortex, and the streamwise and spanwise sizes of the domains are the same. Two simulations for the O_2/H_2 layer are compared with three simulations for the C_7H_{16}/N_2 layer, and the initial conditions of the simulations for the same binary species system differ only by the initial vorticity-thickness-based Reynolds number. All C_7H_{16}/N_2 simulations have reached transitional states, however, only the higher initial Reynolds number O_2/H_2 simulation achieved transition.

Global characteristics of the five layers showed that the momentum thickness and product thickness growth is substantially reduced for the O_2/H_2 layers compared to the C_7H_{16}/N_2 ones. This result is attributed to the much larger initial density stratification of the former layers, which delays entrainment and pairing. The evolution of the global positive spanwise vorticity and of the enstrophy displayed a large peak following the first pairing. However, whereas the global positive spanwise vorticity continued to increase for the C_7H_{16}/N_2 simulations leading to a larger peak at or thereafter the second pairing, it proceeded to decrease for the transitional O_2/H_2 layer; this was a first indication that the turbulence level of the O_2/H_2 layer is reduced with respect to the comparable C_7H_{16}/N_2 layer.

Comparisons of visualizations of the density gradient magnitude non-dimensionalized by the initial value based on conditions at the boundary between the two species, revealed that at transition, previously identified regions of high density-gradient magnitude are stronger but narrower for C_7H_{16}/N_2. These high density-gradient magnitude regions were previously shown to form due both to the distortion of the initial density stratification boundary and to the mixing of the species. The stronger but narrower high density-gradient magnitude regions for C_7H_{16}/N_2 were here attributed to the reduced solubility and mixture non-ideality when compared to the O_2/H_2 system. Since it has been observed that a sharp density stratification is very effective at damping turbulent eddies, we have identified thermodynamic processes (i.e. solubility and mixture

ideality) that affect turbulent development.

Confirmation of the importance of thermodynamic processes in supercritical turbulence came from inspection of the irreversible entropy production (i.e. the dissipation) for the two binary species systems; the locations of maximum dissipation were previously shown to occur within the high density-gradient magnitude regions. The maximum dissipation level is larger for the O_2/H_2 layer consistent with the lower turbulence levels detected from the global analysis, this being attributed to the wider regions of high density-gradient magnitude. However, the largest dissipation is located for the O_2/H_2 layer within regions originating from the distortion of the original density stratification boundary, and for the C_7H_{16}/N_2 layer within regions created through mixing. This difference is traced to the larger solubility and the near mixture-ideality of the O_2/H_2 that creates relatively weak high density-gradient magnitude regions through mixing, and therefore these regions induce a relatively weak dissipation.

To further understand the origin of the different locations of the highest dissipation for the two species systems, budgets of the dissipation in homogeneous planes were compared. In previous investigations it was shown that independent of the species system, at transition, the dissipation in supercritical mixing layers is dominated by the contribution from the species mass flux, with the contribution from viscous and thermal effects being much smaller. Consistent with the finding regarding the location of the regions of highest dissipation in the layer, the budget of the dissipation shows that the maximum peak of the plane average species mass flux contribution is located in the O_2 stream for the O_2/H_2 layer and in the N_2 stream for the C_7H_{16}/N_2 layer. This result is again related to the difference in solubility between the two species systems, as well as to C_7H_{16}/N_2 departures from mixing ideality.

Acknowledgment

This work was conducted at the Jet Propulsion Laboratory (JPL), California Institute of Technology and sponsored by the National Aeronautics and Space Administration (NASA), Marshall Space Flight Center under the direction of Dr. John Hutt, by the Air Force Office of Scientific Research under the direction of Dr. Julian Tishkoff, and by the Army Research Office under the direction of Dr. David Mann, through interagency agreements with NASA. The computational resources were provided by the JPL Supercomputing Center.

[1] Prausnitz, J., Lichtenthaler, R. and de Azevedo, E., *Molecular Thermodynamics for Fluid-phase Equilibrium*, Prentice -Hall, Inc., 1986

[2] Hirshfelder, J. O., Curtis, C. F. and Bird, R. B., *Molecular Theory of Gases and Liquids*, John Wiley and Sons, Inc., 1964

[3] Chehroudi, B., Talley, D. and Coy, E., Initial growth rate and visual characteristics of a round jet into a sub- to supercritical environment of relevance to rocket, gas turbine and Diesel engines AIAA 99-0206, 1999

[4] Mayer, W., Schik, A., Schweitzer, C. and Schaffler, M., Injection and mixing processes in high pressure LOX/GH2 rocket combustors AIAA 96-2620, 1996

[5] Mayer, W., Ivancic, B., Schik, A. and Hornung, U., Propellant atomization in LOX/GH2 rocket combustors AIAA 98-3685, 1998

[6] Oschwald, M. and Schik, A., Supercritical nitrogen free jet investigated by spontaneous Raman scattering *Experiments in Fluids,* 27:497–506, 1999

[7] Bellan, J. and Harstad, K., An all-pressure fluid-drop model: validation and species system dependency, paper presented at the JANNAF Meeting, Destin, Florida, April 8-12, 2002

[8] Miller, R. S., Harstad, K. and Bellan, J., Direct Numerical Simulations of supercritical fluid mixing layers applied to heptane-nitrogen, *J. Fluid Mech.*, 430:1–39, 2001

[9] Okong'o, N. and Bellan, J., Direct Numerical Simulation of a transitional supercritical mixing layer: heptane and nitrogen, accepted for publication in the *J. Fluid Mech.*, 2002

[10] Okong'o, N., Harstad, K. and Bellan, J., Direct Numerical Simulations of O2/H2 Temporal Mixing Layers under Supercritical Conditions, in press, *AIAA J.*, 2002

[11] Sarman, S. and Evans, D. J., Heat flux and mass diffusion in binary Lennard-Jones mixtures, *Phys. Rev.,* A45(4):2370–2379,1992

[12] Harstad, K. and Bellan, J., An all-pressure fluid-drop model applied to a binary mixture: heptane in nitrogen, *Int. J. Multiphase Flow,* 26(10): 1675–1706, 2000

[13] Harstad, K., Miller, R. S. and Bellan, J., Efficient high-pressure state equations, *A.I.Ch.E. J.*, 43(6):1605–1610, 1997

[14] Harstad, K., and Bellan, J., Isolated Liquid Oxygen Drop Behavior in Fluid Hydrogen at Rocket Chamber Pressures, *Int. J Heat and Mass Transfer*, 41:3537–3550, 1998

[15] Harstad, K. and Bellan, J., The D^2 Variation for isolated LOX drops and polydisperse clusters in hydrogen at high temperature and pressures, *Combustion and Flame*, 124:535–550, 2001

[16] Okong'o, N. and Bellan, J., Consistent boundary conditions for multicomponent real gas mixtures based on characteristic waves, in press in the *J. Comp. Phys.*, 2002

[17] Kennedy, C. A. and Carpenter, M. H., Several new numerical methods for compressible shear-layer simulations *App. Num. Math.*, 14:397–433, 1994

[18] Muller, S. M. and Scheerer, D., A method to paralleleize tridiagonal solvers, *Parallel Computing*, 17:181–188, 1991

[19] Okong'o, N. and Bellan, J., Linear stability analysis of supercritical two- and three-dimensional mixing layers, submitted for publication to *Phys. Fluids*, 2001

[20] Moser, R. D. and Rogers, M. M., The three-dimensional evolution of a plane mixing layer: pairing and transition to turbulence, *J. Fluid Mech.*, 247: 275–320, 1993

[21] Moser, R. D. and Rogers, M. M., Mixing transition and the cascade to small scales in a plane mixing layer, *Phys. Fluids* A, 3(5):1128–1134, 1991

[22] Cortesi, A. B., Smith, B. L., Yadigaroglu, G. and Banerjee, S., Numerical investigation of the entrainment and mixing processes in neutral and stably-stratified mixing layers, *Phys. Fluids* 11(1):162–185, 1999

[23] Hannoun, I., Fernando, H. and List, E., 1988 Turbulence structure near a sharp density interface *J. Fluid Mech.*, 189:189–209, 1988

[24] Briggs, D. A., Ferziger, J. H., Koseff, J. R. and Monismith, S. G., Turbulent mixing in a shear-free stably stratified two-layer fluid *J. Fluid Mech.*, 354:175–208, 1998

[25] Okong'o, N. and Bellan, J., Entropy production of emerging turbulent scales in a temporal supercritical n-heptane/nitrogen three-dimensional mixing layer, *Proc. Comb. Inst.*, 28:497–504, 2000

[26] Harstad, K. and Bellan, J., Evaluation of commonly used assumptions for isolated and cluster heptane drops in nitrogen at all pressures, *Combustion and Flame*, 127(1–2):1861–1879, 2001

Species	m (g/mol)	T_c (K)	p_c(MPa)	v_c(cm^3/mol)	Z_c
Hydrogen	2.0159	33.0	1.2838	64.284	0.306
Nitrogen	28.013	126.26	3.399	89.8	0.290
Oxygen	31.9988	154.58	5.0430	73.368	0.288
Heptane	100.205	540.2	2.74	432.0	0.263

Table 1: Pure species properties.

	$\rho_2/\rho_1 = 1$		$\rho_2/\rho_1 = 12.88$		$\rho_2/\rho_1 = 24.40$	
Mean	$x_2 = -\infty$ (O_2)	$x_2 = \infty$(O_2)	$x_2 = -\infty$ (O_2)	$x_2 = \infty$(H_2)	$x_2 = -\infty$ (O_2)	$x_2 = \infty$(H_2)
$\bar{u}_1$(m/s)	-193.732	193.732	-187.287	666.798	-158.004	770.983
a_s(m/s)	484.329	484.329	467.045	1671.193	397.517	1915.376
$\bar{\rho}$(kg/m^3)	63.191	63.191	68.271	5.298	96.764	3.965
p(atm)	100	100	100	100	100	100
T(K)	600	600	556	444	400	600
Y_O	1	1	1	0	1	0

Table 2: Mean flow properties for various values of ρ_2/ρ_1.

Run	Re_0	$L_1 \times L_2 \times L_3$	$N_1 \times N_2 \times N_3$	$\mathrm{Re}_{m,tr}$	t^*_{tr}	max Re_m	$t^*_{\max}$	Timesteps	CPU(h)
R600oh	600	0.2×0.232×0.12	288×336×176	-	-	1195	175	5150	7132
R750oh	750	0.2×0.2×0.12	352×352×208	1507	150	1680	191	6860	13214
R400hn	400	0.2×0.232×0.12	192×224×112	972	150	980	195	3850	878
R500hn	500	0.2×0.232×0.12	240×288×144	1250	155	1471	223	5539	2699
R600hn	600	0.2×0.232×0.12	288×336×176	1452	135	1453	157	4729	5156

Table 3: Listing of the simulations and associated resolution for O_2/H_2 (oh) and C_7H_{16}/N_2 (hn) mixing layers. L_i is in meters. For all layers, $M_{c,0}$ = 0.4 and $\delta_{\omega,0}$= 6.859×10^{-3} m. The other initial conditions were: for O_2/H_2, T_2= 400 K, T_1 = 600 K, p_0 = 100 atm, ρ_2/ρ_1= 24.40; for C_7H_{16}/N_2, T_2= 600 K, T_1 = 1000 K, p_0 = 60 atm, ρ_2/ρ_1= 12.88. All layers transitioned, with the exception of R600oh. The subscript tr denotes the transitional time.

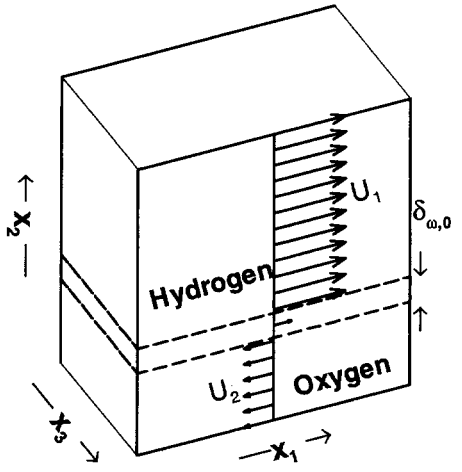

Figure 1: Sketch of the O_2/H_2 mixing layer configuration.

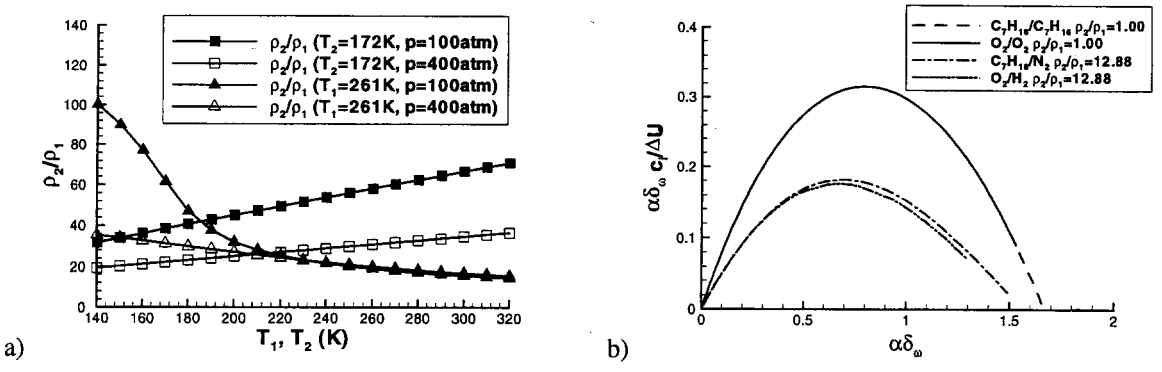

Figure 2: (a) ρ_2/ρ_1 versus T_1 and T_2 for O_2/H_2 at different conditions (b) Comparison of the stability curves for C_7H_{16}/N_2 and O_2/H_2 for $\rho_2/\rho_1 = 1$ and 12.88,.

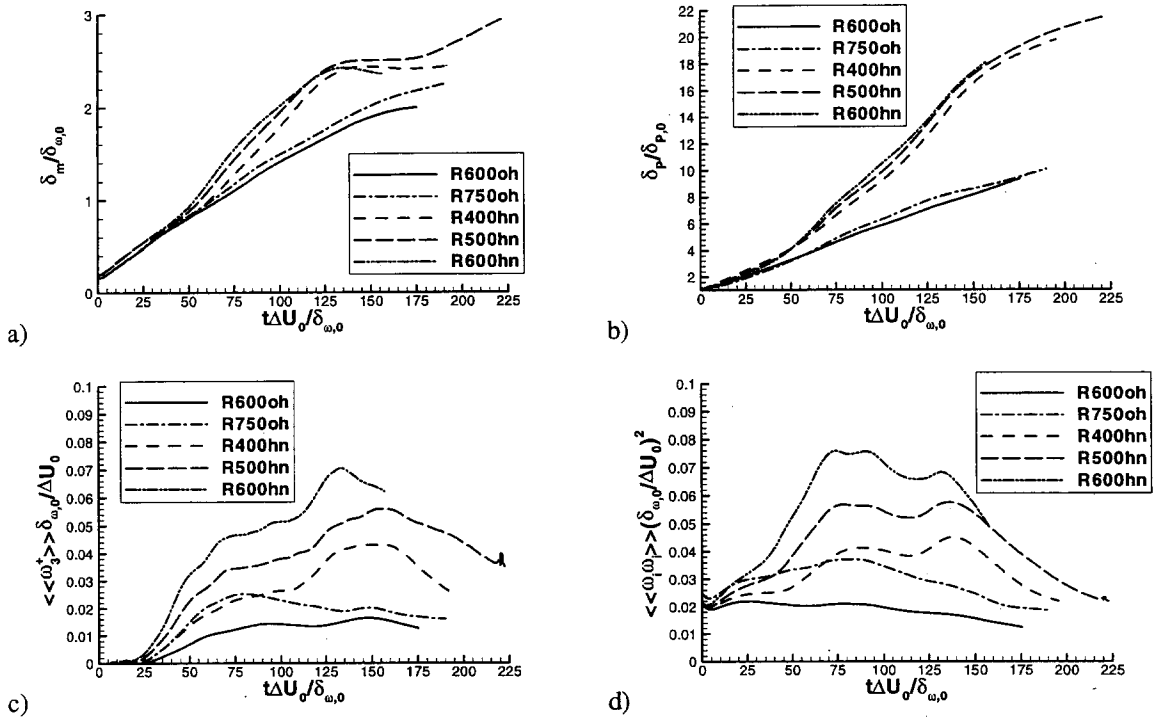

Figure 3: Non-dimensionalized (a) momentum thickness, (b) product thickness, (c) global positive spanwise vorticity, and (d) enstrophy, all versus $t^* = t/(\Delta U_0/\delta_{\omega,0})$.

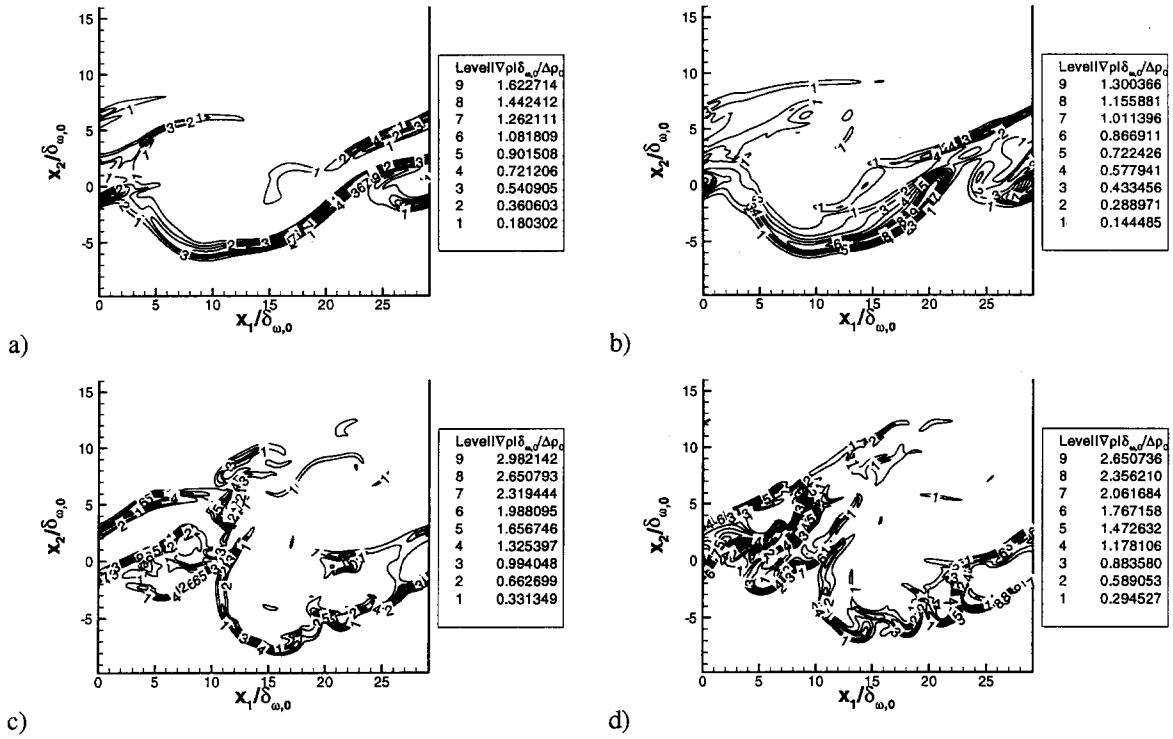

Figure 4: Non-dimensionalized density gradient magnitude for R750oh at t^*=150 (a,b) and for R600hn at t^*=135 (c,d); in the braid plane (x_3=0.0075m) (a,c) and in the between-the-braid plane (x_3=0.06m) (b,d).

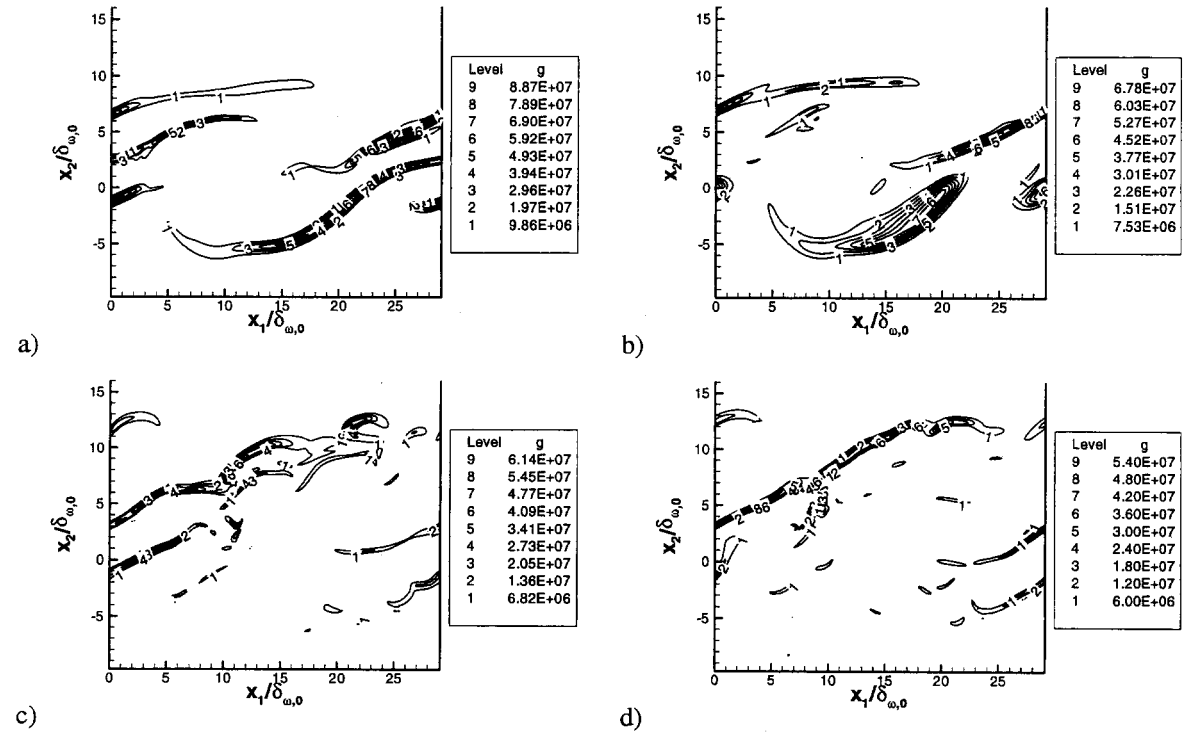

Figure 5: Dissipation (in J/m^{3}K) for R750oh at t^*=150 (a,b) and for R600hn at t^*=135 (c,d); in the braid plane (x_3=0.0075m) (a,c) and in the between-the-braid plane (x_3=0.06m) (b,d).

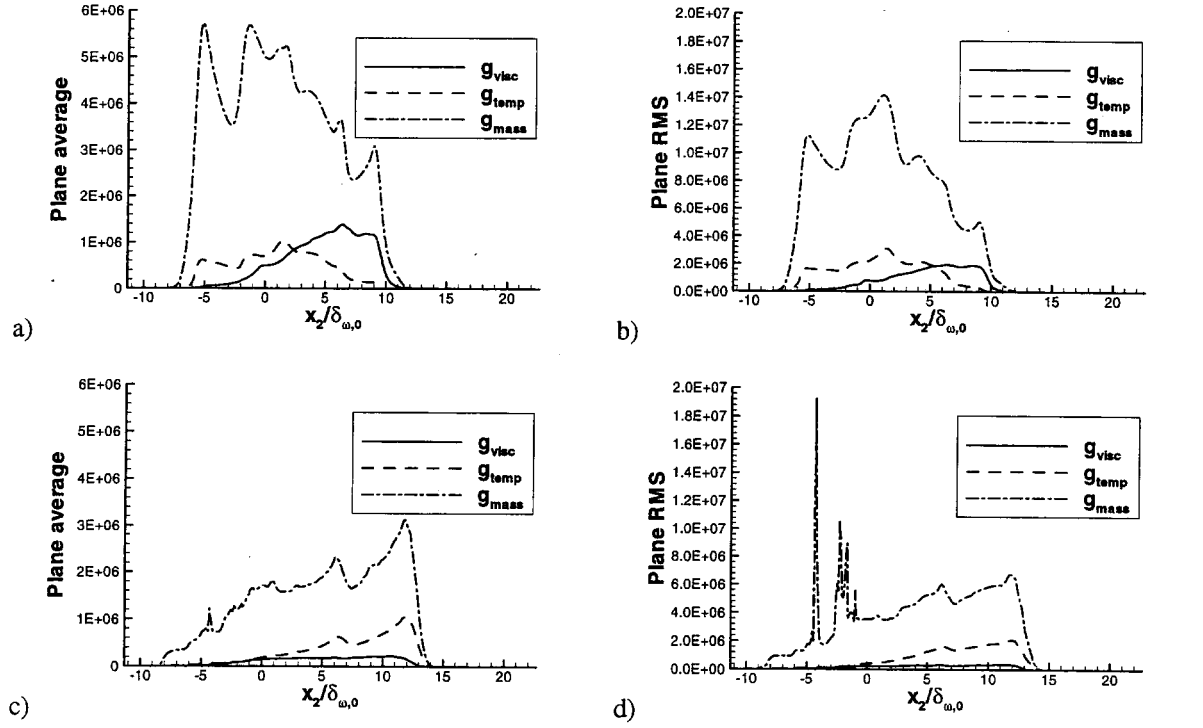

Figure 6: Contributions to the dissipation (in J/m^{3}K) from viscous, molar flux and heat flux effects for R750oh at t^*=150 (a,b) and for R600hn at t^*=135 (c,d); averages (a,c) and RMS (b,d) in homogeneous planes.